Floating on Oil

Jihua Zhang[1, 2]‡*, Xu Deng*[1]‡*, H.-J. Butt*[1]* and Doris Vollmer*[1]*

[1] Max Planck Institute for Polymer Research, Ackermannweg 10, 55128 Mainz, Germany.

[2] Aerospace Research Institute of Material and Processing Technology, Nandonghongmen Road 1, 100076 Beijing, P. R. China.

J. Zhang and X. Deng are equal first authors.

KEYWORDS: fibers, capillary rise, meniscus, wetting, contact angle

ABSTRACT: We demonstrate that disk-shaped steel meshes coated with a superamphiphobic layer are able to float not only on water but also on organic liquids. A coated disk-shaped steel mesh of 1 cm radius has a loading capacity of 17 mN in water and still remarkable 9 mN in *n*-hexadecane. Experimentally measured supporting forces and loading capacities agree well with theoretical predictions. Inspired by the giant water lily, pan-shaped "oil lilies" with even higher loading capacity and artificial oil striders carrying more than ten times their own weight are designed. Even after the artificial devices are fully immersed into different liquids, they show self-draining properties due to capillary forces.

1. INTRODUCTION

Small objects are able to float on water even if their density is higher than that of water. For example, a thin needle floats when carefully placed horizontally on a water surface. If the contact angle of the object and the liquid is significantly above 90°, capillary forces keep the object at the surface. Only when the object becomes too heavy capillary forces are overcome and the object sinks. Some semiaquatic insects and spiders, such as water striders [1-3], utilize capillary forces to walk on water without sinking. This effect has also been applied for the production of artificial water striders [4-8] or miniature boats floating on water [9, 10]. In addition, artificial striders have been made that are able to float at the oil/water interface [11, 12]. Semiaquatic insects and spiders, however, sink if placed on an oil layer.

In contrast, objects are only able to float on oil if their density is below that of the liquid and buoyancy keeps it at the surface. Reasons are that firstly, no planar smooth surface forms a contact angle above 90° with any nonpolar liquid in air. Roughness decreases the contact angle of an oleophilic surface even further. Therefore, wetting is energetically favored. Secondly, the surface tension of a nonpolar liquid is typically 0.020–0.040 N/m rather than 0.072 N/m for water or 0.05 N/m for the water/oil interface. Therefore, capillary forces should be too small to keep a macroscopic object floating. However, here we demonstrate that disk-shaped steel meshes with a superamphiphobic coating or artificial oil striders are able to float on both water and oil surfaces.

Superamphiphobic layers repel both water and oil. They show an apparent advancing contact angle of 150° and a roll-off angle of a drop (5–10 µL) below 10° for oil and water. Oil repellency requires

overhang morphologies and a low energy surface. Tuteja et al. developed a strategy to fabricate superamphiphobic layers [13]. They used randomly-deposited electrospun fiber mats and fabricated superamphiphobic microhoodoo model layers. Superamphiphobic surfaces have also been fabricated by spray coating, electrodeposition, or electrochemical reactions [14-20]. Recently, our group proved that candle soot can be used as a template to prepare transparent robust superamphiphobic layers [21, 22]. In the present paper, we show the possibility to use superamphiphobic layers to fabricate artificial devices that are able to float on water and oil surfaces and support a load comparable to those of natural water striders.

2. EXPERIMENTAL METHOD

Sample preparation. The stainless steel meshes (Haver & Boecker, Germany) with a crisscross pattern (Figure 1a) had a wire diameter of $d = 25$ μm. The quadratic pores size, w, was 25, 56, and 100 μm and allowed air to pass freely. The meshes were cut into rectangular or circular plates with scissors and cleaned by argon plasma. To coat the mesh with a superamphiphobic layer, they were held above the flame of a paraffin candle, and a layer of 10–20 µm thick soot was deposited. The soot consisted of 30–60 nm diameter carbon particles, which formed a loose network. The soot layers were coated with a silica shell of 20–30 nm thickness by chemical vapor deposition (CVD) of tetraethoxysilane and catalyzed by ammonia. This silica coating was hydrophilic and became superamphiphobic after hydrophobization with tridecafluorotetrahydrooctyl trichlorosilane. The thickness of the deposition layer did not influence the properties as long as the thickness exceeded about 5 µm. For thinner layers the regions where the horizontally and vertically woven wires touched each other might be coated incompletely. For details see Deng et al. [21].

To produce pan-shaped mesh we cut circular disks with a diameter of 20 mm, shaped pan-like, and cleaned by argon plasma. The height of the rim varied between 1.0 mm and 3.0 mm. The pan-shaped meshes were made superamphiphobic using the same method as described for the circular flat disks.

Characterization. Wetting properties of water (Millipore, 18.2 Ω/cm), N,N-dimethylformamide (DMF), peanut oil, and n-hexadecane were analyzed. Their surface tensions were measured by the Wilhelmy plate technique. All experiments were carried out at room temperature. The morphology of the meshes and the superamphiphobic coating was characterized by scanning electron microscopy (low voltage LEO 1530 Gemini, Germany, and SU8000, Hitachi, Japan). The apparent static contact angles (CAs) of droplets were obtained using a Dataphysics OCA10 with video profilometry and the drop shape analysis software (Data Physics Instruments GmbH, Germany). The contour of a droplet was determined by a combination of its side profile and the reflection of light scattered from the drop into the liquid surface. The contact angle was calculated by the tangent method. The value depends on the contrast, the way of deposition and sample history, focusing and lighting, giving rise to an error of a few degrees. To keep the mesh straight while measuring the contact angles we placed a circular superamphiphobic mesh on a flat top cylinder. The radius of the mesh exceeded the radius of the cylinder by at least 4 millimeter. A ring with an inner diameter was put over the mesh and the cylinder, thereby straightening the mesh. The tilting angle at which drops roll off was measured at 3 to 5 positions after depositing a 5 µl water drop in the central region of the superamphiphobic mesh, removing the needle and tilting the stage at a speed of 0.5°/s or 1°/s. Simultaneously the shape of the droplet was recorded. The advancing contact angle was measured with a camera from the side while immersing the object into the liquid. The floating force of meshes on

fluidic surfaces was measured by dynamic contact angle measurement (DCAT11, DataPhysics Instruments GmbH, Filderstadt, Germany). Thus, the superamphiphobic mesh was hung on a microbalance. The mesh was moved down at a speed of 0.05 mm/s until the mesh was immersed into the liquid up to a certain depth. Then the superamphiphobic mesh was elevated to its initial position. All test processes and the data collection were controlled through the software SCAT12 (version 1.01).

3. RESULTS AND DISCUSSION

3.1 Wetting of Superamphiphobic Meshes

Steel meshes with a wire diameter, $d = 25$ µm, and different pore sizes, w (25, 56 or 100 µm) were coated with a superamphiphobic layer. Scanning electron microscope (SEM) images show the porous structure of the superamphiphobic layer (Figure 1 a–c). Water drops deposited on the superamphiphobic layer, displayed an apparent contact angle of $168 \pm 4°$ and a roll-off angle $\leq 2°$. The apparent static contact angle for the investigated organic liquids (DMF, peanut oil, and n-hexadecane) varied between $155 \pm 3°$ for n-hexadecane and $165 \pm 4°$ for DMF. The roll-off angles were always well below $10°$ (Figure 1d). The apparent contact angles and roll-off angles were independent of the pore size, w, of the mesh (Figure 1a, supporting information).
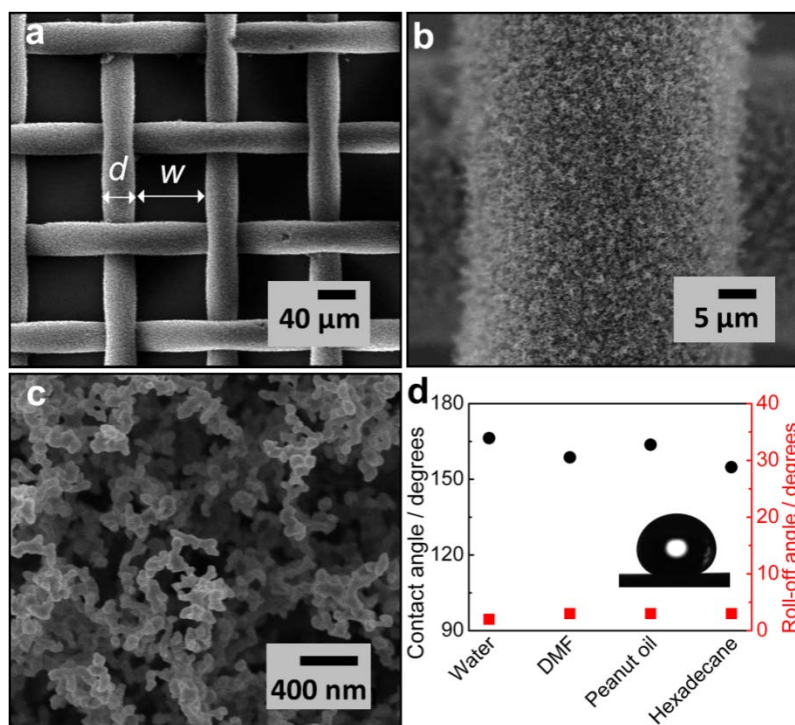

Figure 1. (a–c) Scanning electron microscope (SEM) images of a superamphiphobic mesh taken at different resolutions; (d) Contact angle and roll-off angle of 8 µL liquid drops deposited on the superamphiphobic mesh.

A superamphiphobic mesh was able to float if carefully placed on the surface of n-hexadecane. Its wetting properties were characterized by depositing a drop of water, DMF, peanut oil, and n-hexadecane onto the

floating superamphiphobic mesh (Figure 2a). Even a drop of *n*-hexadecane displayed an apparent static contact angle above 155°. Moreover, the drops easily rolled off when the floating mesh was slightly agitated. The superamphiphobic mesh also remained dry after immersion in *n*-hexadecane (Figure 2b). The silvery shine surrounding the immersed mesh verifies the presence of entrapped air. Thus, the super-amphiphobic layer prevents *n*-hexadecane from infusing the mesh even if the mesh is submerged and acts as a barrier to separates the liquid placed on top from the liquid below. For comparison, meshes that were only hydrophobized with semi-fluorinated silane were investigated. *n*-Hexadecane immediately wetted the mesh and sank into the *n*-hexadecane subphase. To study the liquid repellency, water and *n*-hexadecane drops were jetted on the superamphiphobic mesh floating on water (Figure 2c). The drops bounced off the floating meshes without leaving a trace.

Figure 2. Superamphiphobic meshes floating on liquid. (a) Drops (5 µL) of DMF (white), peanut oil (yellow), *n*-hexadecane (red), and water (blue) deposited onto the superamphiphobic mesh floating on *n*-hexadecane. For better visualization, the drops and the *n*-hexadecane subphase were dyed with oil red O; (b) A superamphiphobic mesh is pushed into *n*-hexadecane; (c) Water drops jetted on a superamphiphobic mesh floating on water.

3.2 Supporting Force

To measure the supporting force a flat disk-like superamphiphobic mesh was slowly immersed into water (Figure 3a) by a circular piston. At the same time, the shape of the water–mesh–air interface (Figure 3b–f) and the supporting force (Figure 3g–h) were recorded. An air-meniscus formed above and around the mesh, which is due to the pronounced water-repellency of the superamphiphobic layer. When the mesh was gradually pushed into the water, the actual angle increased from zero (mesh at the same level as the water surface, $H = 0$, Figure 3b) up to a critical angle of $165° \pm 3°$ at an immersion depth $H = 4.7$ mm (Fig. 3c–e). The critical angle agreed with the apparent contact angle of water ($168° \pm 4°$) measured with the sessile drop method on the flat mesh. The immersion depth, H, is the height between the horizontal water surface and the top surface of the flat mesh. When the mesh is pushed further into the liquid, the meniscus collapsed (Figure 3e), and the water flooded the top surface of the mesh (Figure 3f).
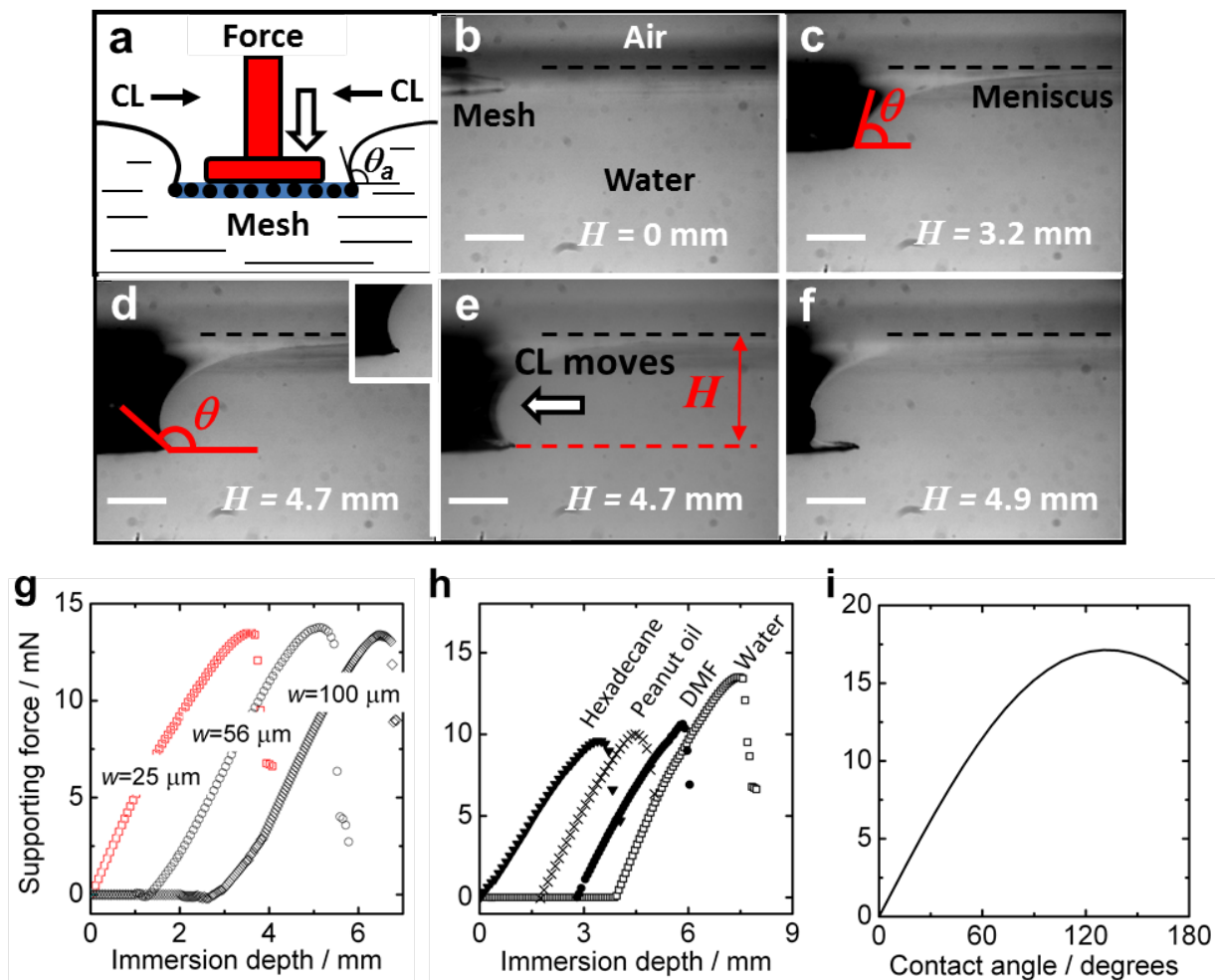
Figure 3. Supporting force. (a) Schematic presentation of the setup. Circular disk-like superamphiphobic meshes with a diameter of 20 mm were used in all cases; (b–f) Series of CCD images of a disk-like superamphiphobic mesh while being immersed into water. The insert in (d) shows the three phase contact line and the shape of the meniscus at higher magnification; (g) Supporting force versus immersion depth for superamphiphobic meshes with different pore sizes, w. The curves were horizontally shifted for better visualization. The error of the immersion depth is about 1 mm and of the force about 2 mN due to problems fixing the superamphiphobic mesh to the piston; (h) Supporting force versus immersion depth for superamphiphobic meshes pressed into water, DMF, peanut oil, and n-hexadecane, $w = 25$ µm, $d = 25$ µm. The curves were horizontally shifted for better visualization. All meshes were pressed into water at a velocity of 0.05 mm/s; (i) Supporting force versus calculated advancing contact angle.

When the mesh was pressed into water, first the supporting force increased almost linearly with the immersion depth (Figure 3g). Just before the meniscus collapsed and the meshes were flooded, the graph of supporting force versus immersion depth reached a maximum and then started to decrease. The sudden decrease of the supporting force after the maximum buoyancy force has been reached indicates flooding.

For a quantitative analysis of the supporting forces, the mesh was treated as a homogeneous circular plate of radius, R, and an advancing contact angle, Θ_a. Capillary forces acting on objects at a liquid surface are a classical problem in capillarity. A mathematically similar problem has, for example, been treated by F. Neumann [23] where the inverse situation was considered: A horizontal circular plate was pulled vertically out of a liquid pond. In the present situation the contact angle has to be replaced by 180° minus the contact angle [23]. In equilibrium, the sum of all forces is zero:

$$F + mg - \rho g \pi R^2 H - 2\gamma \pi R \sin \Theta = 0 \tag{1}$$

F is the load or supporting force applied onto the mesh, m is the mass of the superamphiphobic mesh, $g =$ 9.81 m/s^2 is the gravitational acceleration, γ is the surface tension of the liquid, and ρ is its density. The vertical component of the capillary force $F_c = 2\gamma \pi R \sin \Theta$ and the buoyancy force $F_b = \rho g \pi R^2 H$ act upwards. The gravitational force mg is weak compared to the capillary and buoyancy force, because the meshes are lightweight, $mg = 0.6$ mN. The force required to push the disk into the liquid is equal to the weight of the liquid displaced by the meniscus.

When neglecting the gravitational force, the supporting force depends on the immersion depth H and the actual angle, Θ. Both parameters, immersion depth and contact angle, are linked. When the mesh is pushed into the liquid, H and Θ increase. As the angle increases, the capillary force increases. It increases up to $\Theta = 90°$ after which it decreases again. As the buoyancy keeps increasing, a maximal supporting force is found. To calculate a F-vs-Θ curve and to find the maximal supporting force, a relation between the angle and the immersion depth is needed. Therefore, the Laplace equation would need to be solved numerically to obtain the shape of the liquid meniscus. Good analytical approximations have been found for $R \gg \kappa$, where κ is the capillary constant, $\kappa = \sqrt{\gamma / \rho g}$; for water it is 2.71 mm.

Extrand and Moon derived an approximation for the immersion depth [24]:

$$H = \kappa \sqrt{\frac{2(1 - \cos \Theta)}{1 + \kappa/R}} \tag{2}$$

Inserting Equation 2 into Equation 1 yields for F-vs-Θ:

$$F + mg = 2\gamma \pi R \left(\frac{R}{\kappa} \sqrt{\frac{1 - \cos \Theta}{2(1 + \kappa/R)}} + \sin \Theta \right) \tag{3}$$

A force curve, F-vs-H, was calculated for water with $\rho = 997$ kg/m^3, $R = 0.01$ m and $\gamma = 0.072$ N/m (Figure 3i). The maximal supporting force, i.e., loading capacity, is reached at an immersion depths of 4.5 mm at $\Theta = 135°$. Note that the actual contact angle can exceed 135° as its maximum does not determine when the meniscus collapses. The contact line remains pinned at the rim as long as $\Theta \leq \Theta_a$. The calculated loading capacity of 17.0 mN exceeds 28 times the weight of the mesh. The calculated and measured loading capacities are in good agreement. The measured loading capacity of 15 ± 2 mN was slightly lower than the calculated value, because a slight bending of the mesh or deviations from a perfectly horizontal immersion cannot be excluded.

The buoyancy force was independent of the investigated pore sizes between 25 and 100 µm (Figure 3g). This is reasonable because the maximal hydrostatic pressure $\rho g H = 36$ Pa was much lower than the

critical capillary pressure causing wetting of the meshes by the liquid $\gamma/2w = 360$ Pa, even for great pore size ($w = 100$ µm) and high surface tension $\gamma = 0.072$ N/m.

3.3 Superamphiphobic Meshes Floating on Organic Liquids.

When the disk-like superamphiphobic meshes were placed onto organic liquids, the maximum supported force and immersion depth decreased with the interfacial tension of the liquid (Table 1, Figure 3h). In case of n-hexadecane, the maximum supporting force decreased compared to water by almost 40% to 9 ± 2 mN. However, even in n-hexadecane the loading capacity of the superamphiphobic meshes exceeded 15 times its gravitational force corresponding to $m = 60$ mg.

Table 1. Surface tension, capillary constant, contact angle, and loading capacity calculated with Equation 1 and 2 for the different liquids used; $T = 25$ °C. The error of the experimental loading capacities is ± 2 mN. The critical contact angle and the maximum loading capacity are close to the listed values when calculated with the Neumann approximation, Table S1, [23].

	γ (mN/m)	κ (mm)	Θ_{max} calc.	F_{max} (mN) calc.	F_{max} (mN) exp.
Water	72.0	2.71	132°	16.9	15
DMF	36.4	1.98	141°	11.4	10
Peanut oil	35	1.96	141°	10.9	9
n-Hexadecane	27.1	1.89	142°	8.8	9

3.4 Pan-shaped Disks

The giant water lily (Figure 4a), which can support the body mass of a child, inspired us in the design of our "floating disk". However, one difference between the disk-like superamphiphobic meshes and the natural giant water lily is the rim surrounding the leaf edge. This gives the leaf a "pan-shaped" appearance. To explore the effect of the rim on the wetting behavior and loading capacity, we designed similar structures by fabricating "pan-shaped" superamphiphobic meshes, which we refer to as "oil-lilies" (Figure 4b). When immersing the "pan-shaped" superamphiphobic mesh (PSM) into water, the meniscus moved up the rim of the PSM (Figure 4c). As the water reached the upper edge of the rim ($H = 3.20$ mm, Figure 4d), the contact line was pinned while the meniscus rose above the top of the rim. When further pushing the PSM into the liquid, the meniscus height and the actual contact angle increased (Figure 4e). Notably, the actual contact angle reached 180° according to the Gibbs criterion. We never observed such large contact angles when immersing a flat substrate into water. On a flat disk, the actual contact angle was limited by the apparent advancing contact angle. Immersing the PSM even deeper induced depinning of the contact line (Figure 4f). The meniscus collapsed, and the PSM was flooded by water (Figure 4g).

The loading capacity and the maximal immersion depth, H_{max}, increased with the height of the rim, h, and decreased with the interfacial tension (Figure 4k, 4l). The dependence of the loading capacity and the

maximal immersion depth on the height of the rim can be calculated by Equation 1–3 by adding the rim height to the immersion depth obtained from Equation 2. For increasing immersion depth, the measured loading capacity (Figure. 4k, symbols) slightly exceeded the calculated values (Figure 4k, solid line). This is possibly caused by the shape of the PSMs; the top rim slightly exceeded their bottom diameter, $2R$ (Figure 4g).

When lifting a fully immersed PSM, the water layer ruptured a few millimeters before the top side of the walls reached the water surface (Figure 4h) and the meniscus reformed. Capillary force induced dewetting, leaving the PSM dry (Figure 4i, j, Video S1). The flooding and self-drainage cycle of the artificial lilies can be repeated several times (Video S2). To quantify the self-draining of the PSM, we measured the supporting force for a full immersion-lifting cycle (Figure 4m). The PSM was pushed under water; the sudden decrease of the supporting force marks the collapse of the meniscus, followed by the flooding of the PSM. The PSM is now fully engulfed by water. The supporting force remained well below zero, as air was entrapped in the superamphiphobic mesh. After starting to lift the PSM, the supporting force decreased. At $H \approx 3.1$ mm, just above the capillary length of 2.71 mm, the water layer covering the PSM ruptured, and the capillary force pulled the water off the PSM. No water was left within the PSM, as the supporting force for lifting and immersion fall on top of each other. In analogy to the giant water lily, the low margin height of the PSM keeps it dry, even after flooding with water.
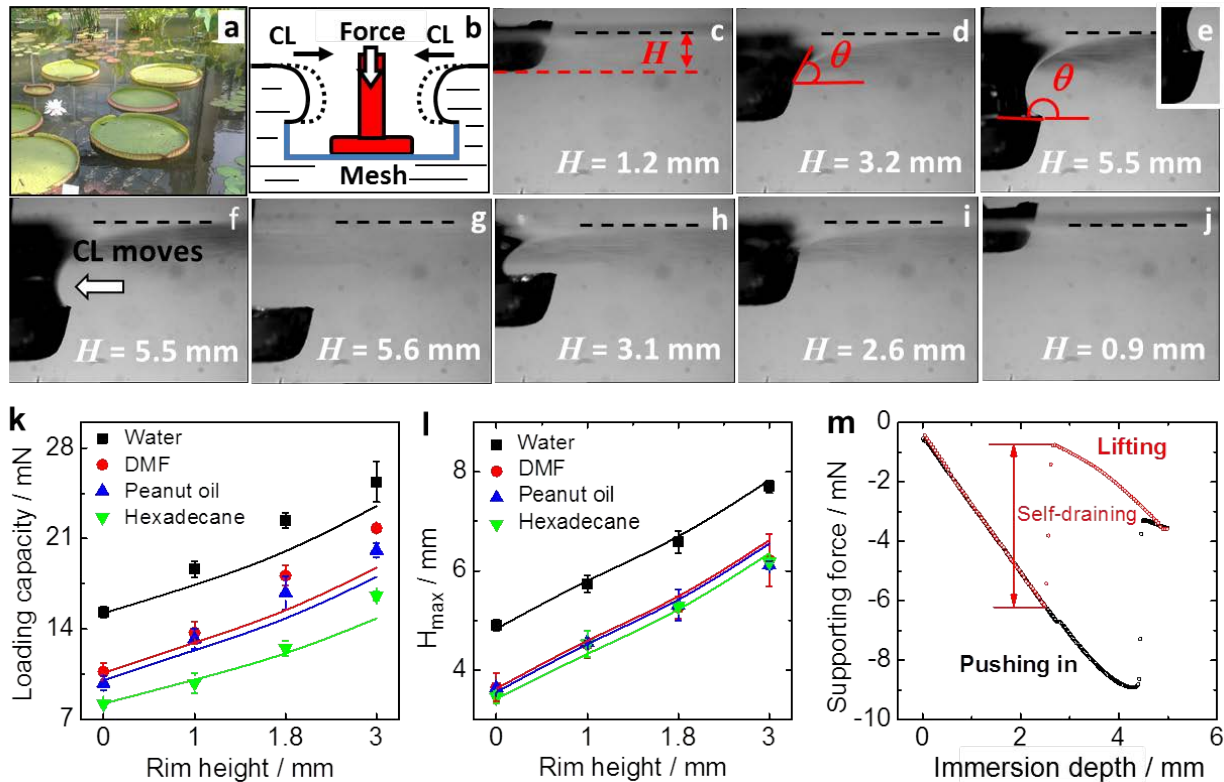

Figure 4. Pan shaped meshes. (a) Giant water lilies; (b) Schematic setup; (c–j) Sequence of images showing a superamphiphobic pan-shaped mesh while being pushed into and pulled out of water. The insert in (e) shows the three phase contact line and the shape of the meniscus at higher magnification; (k) Loading capacity versus rim height for different liquids, solid lines were calculated with Equation 3; (l) Maximal immersing depth versus the rim height for different liquids; lines were added for better

visibility. The error of the loading capacity is about 2 mN and of the maximal immersing depth about 1 mm due to problems fixing the meshes to the piston. (m) Supporting force versus position, for a single pan-shaped superamphiphobic mesh.

3.5 Oil strider

Inspired by the water strider, we designed a model device using four PSMs as "legs", which we refer to as "oil strider" (Figure 5a, 5b). The artificial oil strider was able to move freely on the water surface or was guided by applying a permanent magnet that was placed over or under the water container. The four ferric "legs" of the oil strider followed the horizontal motion of the magnet (Video S3). In contrast to its natural counterpart, the oil strider was also able to float on organic liquids (Figure 5c). After removing the oil strider off the liquid, neither residual water nor organic liquid adhered to the "legs".

To investigate its floating capacity on oil-polluted surfaces, we poured peanut oil on the water surface and around the legs of the oil strider while it was floating on the surface (Figure 5b). The oil/water interfaces can be clearly distinguished due to their different refractive indices. During the whole process, floating of the device on water was little affected (Video S4). The motion of the oil strider can also be controlled by the magnet on the oil-polluted surface (Video S5). The device moved freely from the water to the oil domains. Even in n-hexadecane with its low surface tension, the four legs bear a supporting force of 18 ± 3 mN. Thus, its loading capacity exceeded 13 times the weight of the "legs" (weight of each leg 0.35 mN)

The floating stability of the device on the liquid surface was tested by agitating the container to wave the oil-polluted surface. The artificial oil strider floated up and down without tilting over, even at 150 rpm (Video S6). After the end of the rocking motion, the device was still dry and stood firmly on the surface. Thus, the oil polluting the water surface had no effect on the floating capability of the oil strider. Indeed, the device was also able to float on organic liquids, although compared to water the floating force and therefore the loading capacity decreased in DMF, peanut oil and n-hexadecane (Figure 5c).
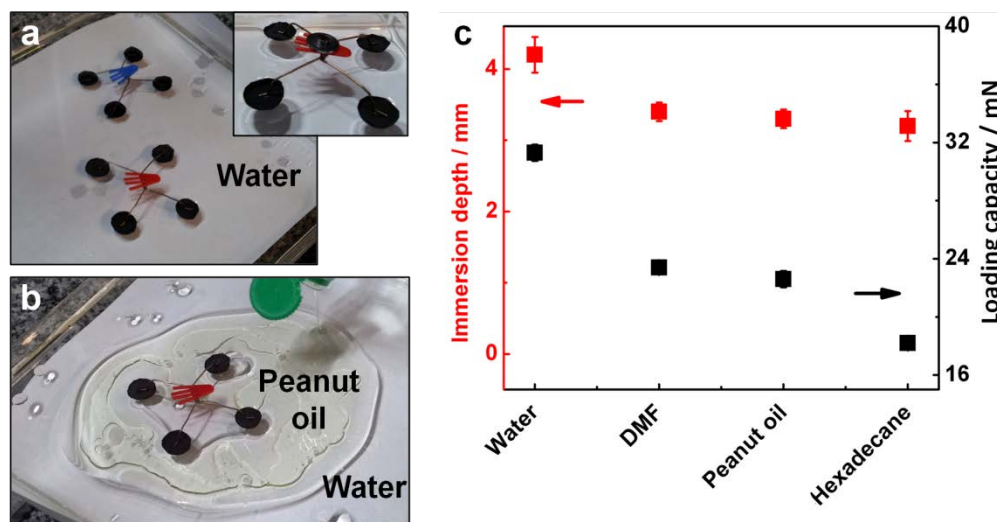

Figure 5. (a) Artificial oil striders floating on a water surface. Inset: enlarged view of an oil strider bearing an extra weight of 0.8 g; (b) Oil strider moving on an oil-contaminated surface. The four spherical

pan-shaped legs had a diameter of 12.5 mm and a rim height of 1 mm; (c) Maximal immersing depth and loading capacity of the artificial oil strider on various liquid.

4. CONCLUSION

Lightweight, self-draining artificial oil lilies and oil striders can be constructed from superamphiphobic meshes. The loading capacity of the pan-shaped superamphiphobic devices can be tuned by the height of the rim, as long as the hydrostatic pressure exceeds the capillary pressure of the superamphiphobic mesh. Even a rim height of 1 mm increased the loading capacity of the artificial oil strider to 13 times its own weight. The oil strider moved freely on water and oil surfaces. All devices kept dry and clean even after they were flooded by water or oil.

AUTHOR INFORMATION
Corresponding Author
 *E-mail: butt@mpip-mainz.mpg.de (H.J.B) and vollmerd@mpip-mainz.mpg.de (D.V)

Present Addresses

X.D: Materials Sciences Division of the Lawrence Berkeley National Laboratory, Berkeley, California 94720, USA

1.   Wang, Q., et al., *Modeling and Analysis of the Supporting Force of Water Strider's Legs*, in *Applied Mechanics and Mechanical Engineering Ii, Pts 1 and 2*, H.H. Tan, Editor. 2012. p. 356-361.
2.   Gao, X.F. and L. Jiang, *Water-repellent legs of water striders.* Nature, 2004. **432**(7013): p. 36-36.
3.   Bush, J.W.M. and D.L. Hu, *Walking on water: Biolocomotion at the interface*, in *Annual Review of Fluid Mechanics*. 2006. p. 339-369.
4.   Hu, D.L. and J.W.M. Bush, *Meniscus-climbing insects.* Nature, 2005. **437**(7059): p. 733-736.
5.   Shi, F., Z.Q. Wang, and X. Zhang, *Combining a layer-by-layer assembling technique with electrochemical deposition of gold aggregates to mimic the legs of water striders.* Advanced Materials, 2005. **17**(8): p. 1005-+.
6.   Song, Y.S., et al., *Modeling of the supporting legs for designing biomimetic water strider robots*, in *2006 Ieee International Conference on Robotics and Automation*. 2006. p. 2303-2310.
7.   Jiang, L., et al., *"Water Strider" Legs with a Self-assembled Coating of Single-Crystalline Nanowires of an Organic Semiconductor.* Advanced Materials, 2010. **22**(3): p. 376-+.

8.   Shi, F., et al., *Towards understanding why a superhydrophobic coating is needed by water striders.* Advanced Materials, 2007. **19**(17): p. 2257-+.

9.   Pan, Q. and M. Wang, *Miniature Boats with Striking Loading Capacity Fabricated from Superhydrophobic Copper Meshes.* Acs Applied Materials & Interfaces, 2009. **1**(2): p. 420-423.

10.   Xiao, M., et al., *pH- Responsive On- Off Motion of a Superhydrophobic Boat: Towards the Design of a Minirobot.* Small, 2014. **10**(5): p. 859-865.

11.   Liu, X., et al., *Bioinspired Oil Strider Floating at the Oil/Water Interface Supported by Huge Superoleophobic Force.* Acs Nano, 2012. **6**(6): p. 5614-5620.

12.   Zhang, X., et al., *Bioinspired Aquatic Microrobot Capable of Walking on Water Surface Like a Water Strider.* ACS Appl. Mater. Interfaces, 2011. **3**: p. 2630-2636.

13.   Tuteja, A., et al., *Designing superoleophobic surfaces.* Science, 2007. **318**(5856): p. 1618-1622.

14.   Choi, W., et al., *Fabrics with Tunable Oleophobicity.* Advanced Materials, 2009. **21**(21): p. 2190-+.

15.   Meng, H., et al., *Facile means of preparing superamphiphobic surfaces on common engineering metals.* The Journal of Physical Chemistry C, 2008. **112**(30): p. 11454-11458.

16.   Wang, H., et al., *Durable, Self-Healing Superhydrophobic and Superoleophobic Surfaces from Fluorinated-Decyl Polyhedral Oligomeric Silsesquioxane and Hydrolyzed Fluorinated Alkyl Silane.* Angewandte Chemie International Edition, 2011. **50**(48): p. 11433-11436.

17.   Kim, S.-H., S.Y. Lee, and S.-M. Yang, *Janus Microspheres for a Highly Flexible and Impregnable Water-Repelling Interface.* Angewandte Chemie-International Edition, 2010. **49**(14): p. 2535-2538.

18.   Zhang, J. and S. Seeger, *Superoleophobic coatings with ultralow sliding angles based on silicone nanofilaments.* Angewandte Chemie International Edition, 2011. **50**(29): p. 6652-6656.

19.   Zhou, H., et al., *Robust, Self-Healing Superamphiphobic Fabrics Prepared by Two-Step Coating of Fluoro-Containing Polymer, Fluoroalkyl Silane, and Modified Silica Nanoparticles.* Advanced Functional Materials, 2013. **23**(13): p. 1664-1670.

20.   Steele, A., I. Bayer, and E. Loth, *Inherently superoleophobic nanocomposite coatings by spray atomization.* Nano Letters, 2008. **9**(1): p. 501-505.

21.   Deng, X., et al., *Candle soot as a template for a transparent robust superamphiphobic coating.* Science, 2012. **335**(6064): p. 67-70.

22.   Paven, M., et al., *Super liquid-repellent gas membranes for carbon dioxide capture and heart–lung machine.* Nature Communications open access, 2013. **4**: p. 2512.

23.   Neumann, F., *Vorlesungen über die Theorie der Capillarität*, ed. A. Wangerin. 1894, Leipzig: Teubner. 234.

24.   Extrand, C. and S.I. Moon, *Will It float? Using cylindrical disks and rods to measure and model capillary forces.* Langmuir, 2009. **25**(5): p. 2865-2868.